Methyl iodide *A*-band decomposition study by photofragment velocity imaging

André T. J. B. Eppink and David H. Parker
Department of Molecular and Laser Physics, University of Nijmegen, Toernooiveld, 6525 ED Nijmegen, The Netherlands

(Received 17 April 1998; accepted 18 June 1998)

The methyl iodide *A*-band photodissociation process $CH_3I+h\nu \rightarrow CH_3(v,N,K)+I(^2P_{3/2})$, $I^*(^2P_{1/2})$ has been studied in a cold molecular beam. Full three-dimensional state-specific speed and angular distributions of the nascent fragments were recorded using (2+1) resonance-enhanced multi-photon ionization (REMPI) and velocity imaging, a new variant of ion imaging. By combining the I* quantum yield and anisotropy parameters for both I and I* channels, the relative absorption strength to the contributing electronic states ($^3Q_0$, $^3Q_1$ and $^1Q_1$) as well as the probability for curve crossing ($^3Q_0 \rightarrow {}^1Q_1$) are determined for excitation wavelengths across the full *A* band (240–334 nm). Parallel excitation to the $^3Q_0$ state turns out to dominate the *A* band even more than previously thought. © *1998 American Institute of Physics.* [S0021-9606(98)00836-8]

I. INTRODUCTION

The *A*-band photodissociation of CH_3I in the ultraviolet region of the spectrum (220–350 nm) is an important benchmark for the understanding of polyatomic molecule photodissociation for experimental as well as theoretical reasons. Studies of methyl iodide photodissociation have led to important general insights into, e.g., the mechanisms of fragment internal energy disposal, curve crossing, and angular momentum correlation mechanisms. The basis of knowledge on CH_3I has developed steadily over the past three decades into a tremendous body of literature, as recently reviewed by Kinsey and co-workers[1] and others.[2,3]

Still, a hiatus has remained in the experimental characterization of the absorption profile of the *A* band of CH_3I. The absorption spectrum is composed of three broad, optically allowed transitions to dissociative states, which lead to fragmentation into CH_3 and $I(^2P_{3/2})$ or $I^*(^2P_{1/2})$. A decomposition analysis by Gedanken and Rowe,[4] based on a magnetic chromatic dichroism (MCD) measurement, has served as the main guideline for the many superb theoretical efforts for more than two decades, but up to now no systematic alternative decomposition using other experimental methods has been reported. Because the system is very well suited for a photofragment study using more recent techniques, the velocity imaging method in this case, an alternative decomposition has become feasible by studying fragment distributions, which we present in this paper. In comparison with previous investigations, this is a study across the full *A* band using one apparatus, thereby circumventing difficulties in making comparisons between different experimental techniques at different excitation wavelengths. Besides the composition of the *A* band, the velocity imaging measurements reveal many other aspects of the photodissociation process. These aspects, especially the vibrational energy disposal in the methyl radical, are discussed in a separate article.[5]

Since the introduction of ion imaging about ten years ago,[6] the application of imaging techniques in molecular reaction dynamics studies has evolved enormously, as recently reviewed in Refs. 7 and 8. Ion imaging, and especially its latest version velocity imaging,[9] has proven to be quite suitable for detection of the full angle-velocity distributions of photofragments[10] and for measurements of fragment alignment,[11,12] furthermore, the method can be used in crossed beam studies[13] and combined with reactant state selection and orientation.[14] Conventional ion imaging techniques make use of grid electrodes to extract and accelerate the ions toward the detector. In velocity imaging the extracting electric field is built up with an electrostatic lens that projects the ion distribution onto the detector in velocity space. Better image quality results, thus more accurate angular and speed information, both of which are vital for this study.

II. DECOMPOSITION METHOD

In this section we show how a combination of experimental observables can reveal the nature of the initial photon absorption step and the subsequent dissociation processes. As shown schematically in Fig. 1, the *A* band absorption of CH_3I involves three optically allowed transitions from the $X(^1A_1)$ ground state: two weak perpendicular transitions to the $2E$ ($^3Q_1$) and $3E$ ($^1Q_1$) states that correlate to the $I(^2P_{3/2})$ (≡I) channel and a strong parallel transition to the $2A_1$ ($^3Q_0$) state that correlates adiabatically to the $I^*(^2P_{1/2})$ (≡I*) channel, where ($^3Q_0$) is the Mulliken notation,[15] and (A_1,E) the appropriate C_{3v} notation.[16] In accord with the literature, the Mulliken notation will be used for the upper states in this article. The spin-orbit splitting[17] between I and I* is 0.943 eV and a C–I bond energy (D_0) of 2.39±0.03 eV has been determined in translational spectroscopy measurements.[18,19]

The photodissociation of methyl iodide is direct[20] (the dissociation time $\tau_{diss} \sim 0.065$ ps is much smaller than the parent rotation time $\tau_{rot} \sim 1$ ps) and is usually assumed to be an ''axial recoil'' case, for which the C_{3v} symmetry is main-

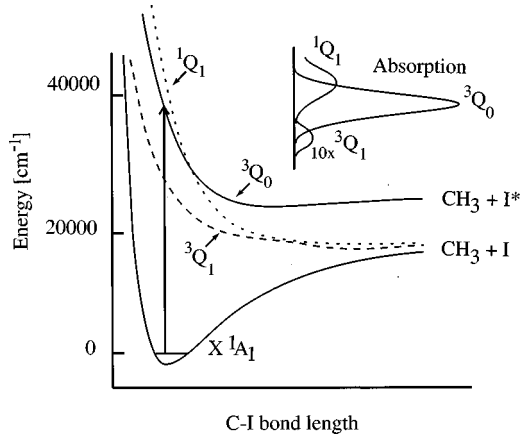

FIG. 1. Schematic view of potential energy surfaces involved in CH_3I *A*-band photodissociation. Deconvoluted absorption curves from Gedanken and Rowe (Ref. 4) are shown schematically. Note that ~17% of the total absorption is assigned in Ref. 4 to the $^1Q_1$ state, which peaks at the high energy end of the spectrum.

tained during the dissociation process. Recent theoretical studies[2] indicate, however, a slight H_3C–I bending during dissociation ($<5°$), which breaks down the C_{3v} symmetry, and allows curve-crossing ($^3Q_0 \rightarrow {}^1Q_1$) involving a nonadiabatic transition at the conical intersection to take place via coupling of the radial derivative terms in the Hamiltonian.[21] The $^3Q_0$ and $^1Q_1$ curves have a crossing point (conical intersection) well outside the Franck–Condon region.[22] For both dissociation limits the corresponding methyl fragment can be produced in numerous rovibrational states. Because the methyl group geometry changes from pyramidal in CH_3I to planar in free CH_3, the umbrella mode of CH_3 is the most extensively excited vibration on C–I bond breaking. The absorption process and subsequent dissociation dynamics are assumed here to be independent, and possible coherence effects due to simultaneous excitation of two electronic states are not considered.

Following photoabsorption, the nascent fragments recoil with a total kinetic energy T_{tot} which is determined by energy conservation:

$$T_{\mathrm{tot}} = h\nu - D_0 - E_{\mathrm{int}}(I) - E_{\mathrm{int}}(\mathrm{CH_3}) \tag{1}$$

with E_{int} the fragment internal energy. Since the methyl rovibrational state distributions are narrower than the splitting of the iodine spin-orbit states, the kinetic energy distribution can be conveniently divided into two channels (I and I*). Momentum conservation leads to a division of this kinetic energy release (KER) among the fragments in a fixed ratio determined by their masses:

$$T_I = \left[\frac{m_{\mathrm{CH_3}}}{(m_{\mathrm{CH_3}} + m_I)}\right] T_{\mathrm{tot}} = \frac{15}{142}\, T_{\mathrm{tot}}, \tag{2a}$$

$$T_{\mathrm{CH_3}} = \left[\frac{m_I}{(m_{\mathrm{CH_3}} + m_I)}\right] T_{\mathrm{tot}} = \frac{127}{142}\, T_{\mathrm{tot}}. \tag{2b}$$

Absorption leads to production of an initial population, N_0^*, of molecules in the I* channel. The population change due to curve crossing can be described by:

$$N^* = (1 - P_{cc}) N_0^*, \tag{3a}$$

$$N = N_0 + P_{cc} N_0^*, \tag{3b}$$

where N and N^* are the final populations in the I and I* channel, respectively, and P_{cc} the probability for curve crossing. By normalizing the total population ($N + N^* = N_0 + N_0^* = 1$) the quantum yields are found, i.e., $\Phi^* = N^*/(N + N^*) = N^*$ after completion of the dissociation process and $\Phi_0^* = N_0^*/(N_0 + N_0^*) = N_0^*$ just after the absorption step.

Using linearly polarized light the angular distribution of photofragments is described by the differential cross section

$$\frac{d\sigma}{d\Omega} = \frac{\sigma}{4\pi}\left[1 + \beta\left(\tfrac{3}{2}\cos^2\theta - \tfrac{1}{2}\right)\right], \tag{4}$$

where θ is the fragment ejection angle relative to the laser polarization axis, σ the integral cross section, and β the anisotropy parameter, $-1 \leqslant \beta \leqslant 2$. For pure parallel transitions the transition dipole moment lies parallel to the C–I bond, which leads to $\mathrm{I}(\theta) \propto \cos^2\theta$, i.e., $\beta = 2$. Similarly, $\beta = -1$ is found for pure perpendicular transitions [i.e., $\mathrm{I}(\theta) \propto \sin^2\theta$] and $\beta = 0$ for isotropic distributions. We assume that the effects of the predicted[2] slight C–I bending motion during dissociation on the resulting angular distribution (β parameter) is negligible, especially since the bending occurs at an increased C–I distance.

The transfer of population ($^3Q_0 \rightarrow {}^1Q_1$) taking place outside the Franck–Condon region is also assumed not to affect the anisotropy in the I* channel. For the I channel, two contributions play a role in determining β, direct (perpendicular) absorption and curve crossing, which may be written

$$\beta = a\beta_{\parallel} + b\beta_{\perp} = a\beta^* + b(-1), \tag{5}$$

which, by taking $a + b = 1$, leads to

$$a = \frac{(1 + \beta)}{(1 + \beta^*)}, \tag{6a}$$

$$b = \frac{(\beta^* - \beta)}{(1 + \beta^*)}. \tag{6b}$$

Here it is assumed that the direct contribution in the I channel has a pure perpendicular character ($\beta_{\perp} = -1$), while the nonadiabatic contribution (originating from $^3Q_0 \rightarrow {}^1Q_1$ crossing) retains the same anisotropy as the fragments that appear in the I* channel ($\beta_{\parallel} = \beta^* \approx 2$).

By making use of the fact that a denotes the fraction in the I channel that originates from the curve-crossing, one finds $N^* = [N_0^* - aN]$ and $N = [N_0 + aN]$ which, using Eq. (3a) or Eq. (3b), leads to:

$$P_{cc} = \frac{aN}{N_0^*} = \frac{a(1 - \Phi^*)}{\Phi_0^*} = \frac{\text{fraction of population that curve crossed}}{\text{fraction of population initially in } {}^3Q_0}. \tag{7}$$

The fraction of the total population that was initially in the $^3Q_0$ state (after optical excitation) is found from

$$\Phi_0^* = \Phi^* + a(1 - \Phi^*). \tag{8}$$

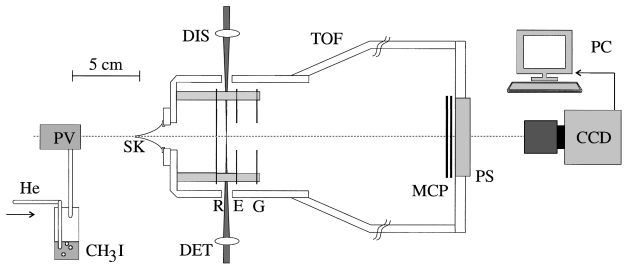

FIG. 2. Velocity imaging experimental setup. PV=pulsed valve; SK=1 mm skimmer; R, E, G=repeller, extractor, and ground electrode; 36 cm TOF tube from laser focus to detector; dual MCP detector with PS=phosphor screen; CCD camera connected to the PC. The dissociation (DIS) and detection (DET) lasers are focused near the molecular beam with 20 cm lenses. Essential distances are drawn to scale.

Thus by combining the experimental quantum yield Φ^* with anisotropy parameters β and β^* the absorption strength to the $^3Q_0$ state relative the to that of the perpendicular states $^1Q_1$ and $^3Q_1$ is revealed for each dissociation wavelength. Since the two perpendicular states are expected to be well separated, the contribution due to the $^3Q_1$ state is extracted at low excitation energies and the $^1Q_1$ at high energies.

III. EXPERIMENT

A. Molecular beam apparatus

The velocity imaging method applied in this study has been described previously in detail[9] and is based upon the application of a three-plate electrostatic immersion lens instead of grid electrodes for the extraction of the ions. This technique provides superior resolution compared to more commonly used grid assemblies. Briefly, as depicted in Fig. 2, a solenoid valve (General Valve) equipped with a 0.8 mm nozzle produces a $\sim$150 μs pulsed molecular beam of CH_3I seeded in He at 1–4 bar stagnation pressures. The mixture is prepared by feeding the carrier gas through liquid CH_3I in a stainless steel bubbler, held at 0 °C to obtain a CH_3I vapor pressure of $\sim$128 Torr and to suppress I_2 contamination. About 40 mm downstream the beam passes a 1 mm diameter skimmer which separates the source and detection chambers; about 100 mm downstream from the nozzle the beam passes through a 1 mm hole in a repeller electrode plate and propagates further along the axis of the 36 cm long time-of-flight (TOF) tube. The three electrodes of the ion lens are 0.2 mm thin stainless steel flat plates of 70 mm diameter. The extractor and ground electrodes have 20 mm diameter apertures which are well matched for lensing with the present TOF length.

Two counterpropagating lasers are used, one for dissociation of the CH_3I between 240 and 333 nm ($<$1 mJ/pulse) and the other for detection ($<$0.1 mJ/pulse) of one of the fragments, i.e., $CH_3(v,J,K)$, $I(^2P_{3/2})$, or $I^*(^2P_{1/2})$. The most complete studies were carried out using a 10 bar H_2 Raman cell to produce Stokes and anti-Stokes shifted components for the dissociation step. Pumping with the fourth harmonic of a Nd:YAG laser (Spectra-Physics, DCR-2A) at 266 nm, the 220, 240, 266, or 300 nm Raman components ($\Delta E = 4156\ cm^{-1}$) were selected with a Pellin–Broca prism. Other dissociation wavelengths were produced using the output of a YAG-pumped dye laser (Spectra-Physics GCR-11 and PDL-1) which was frequency doubled in a KDP crystal.

Upon photodissociation, the fragments spread out radially at a speed which is determined by conservation of energy and momentum. The methyl fragments are probed by (2+1) resonance-enhanced multi-photon ionization (REMPI) through the $3p_z$ Rydberg state,[23] using the 0_0^0 band for probing $CH_3(v=0)$ around 333.45 nm and the 1_1^1, 2_1^1, 2_2^2, and 2_3^3 bands for probing vibrationally excited fragments. Data are mainly recorded on the collapsed Q branches, for which minimal sensitivity to fragment alignment is to be expected.[12] For iodine atoms the REMPI lines[24] are much narrower than the Doppler profile, requiring the wavelength to be scanned back and forth across the transition during data acquisition to ensure a homogeneous detection efficiency. For the methyl radicals detected via the broad Q branch, all velocity groups are detected at equal sensitivity; mainly the peak of the branch was used since no variations in the images are found across the Q branch.

The lasers are focused perpendicular to the TOF axis midway between the repeller and extractor electrode. Both lasers generally have their electric field polarization directions lying parallel to the detector face. The lasers are focused by lenses with focal lengths which are chosen carefully in each case in order to ensure homogeneous detection efficiencies at proper overlap of the foci. A small time delay between the two laser pulses is usually chosen (5–30 ns), and checked for detection homogeneity. The laser flux is attenuated with filters to avoid space charge problems where necessary. The formed ions are accelerated by the extractor electric field into the TOF tube, thereby flattening the spherical ion distribution along the TOF axis and decreasing the spread in time-of-flight to $\Delta t/t < 1\%$. At the end of the TOF tube the ions impinge onto a 40 mm diameter imaging detector, which consists of a dual microchannel plate (MCP)/P-20 phosphor combination (Galileo, FM-3040). Mass selectivity is obtained by applying a timed voltage pulse with a HV switch on the front MCP, thus gating the gain to select ions with a particular time-of-flight. The 2D images on the phosphor screen are recorded using a Peltier-cooled CCD camera (LaVision, 384×286 pixels) equipped with a $f=25$ mm objective (Schneider) and stored in a 486PC where further data analysis can be performed. Due to the ion lens functionality, these images represent a projection of the ion distribution in velocity space; blurring of the image caused by the spatial extension of the ionization volume (i.e., overlap volume between ionization laser focus and molecular beam) is thus avoided. By choosing the polarization of the dissociation laser (i.e., axis of cylindrical symmetry) parallel to the imaging plane, the full 3D velocity distributions can be reconstructed from the images by means of an inverse Abel transform.[7]

Problems due to cluster formation are avoided by firing the lasers in the early part of the molecular beam pulse. CH_3 and I signals due to clusters have a low kinetic energy release and show up as ''blobs'' in the middle of the image. At dissociation wavelengths around 220 nm the only significant CH_3^+ or I^+ signals are due to clusters, and not, within our sensitivity range, due to monomer dissociation. As deter-

mined from O_2 photodissociation studies,[9,10] the velocity resolution (i.e., the apparatus function) is limited by the spatial resolution obtainable with the MCP-CCD detection system: single ion events show up as 0.15 mm diameter spots on the phosphor screen, while the CCD camera is usually set at ~0.10 mm per pixel. Typically this results in a 30 meV resolution at 1 eV kinetic energy release.

B. Ion lens performance

The application of open electrode configurations in ion and electron imaging applications has been described previously.[9] The last lens electrode is held at ground and the repeller and extractor voltages (V_R,V_E) are optimized for image size and sharpness. Due to the lens functionality, a 100% ion transmission is reached without distortions common in conventional ion imaging using grid electrodes (trajectory deflections and blurring effects), leading to images that represent a 2D velocity map (i.e., a flat projection in velocity space) of the 3D ion distribution with a high spatial resolution of the image. As the ratio V_E/V_R is set and fixed for optimal velocity mapping ($V_E/V_R=0.71$ for our 36 cm TOF tube), images in any size desired can be obtained for any ion mass (or electrons) by changing the repeller voltage. The radius R in the 3D fragment distribution behaves as $R=Nvt$, with v the fragment recoil speed, t the time-of-flight, and N a uniform and constant magnification factor ($N=1.29$ for a 36 cm TOF length). The value of N is easily experimentally confirmed by processes with known kinetic energy release (''external'' calibration) or by comparing known dissociation channels at different radii (''internal'' calibration). This proportionality of radius with speed indicates the same close relation between image and fragment velocity distribution. It is found that the t follows a standard TOF dependence with repeller voltage V_R and fragment mass m and charge q, i.e., $t\propto[(m/(qV_R)]$, which simplifies the ion mass identification. This also leads to the mass independent relation:

$$R\propto N[T/(qV_R)]^{1/2}, \tag{9}$$

where T is the kinetic energy of the fragment. This enables a direct comparison of images extracted from different masses; particles having kinetic energy of 1 eV appear always at the same radius in the image, independent of the mass of the particle. As shown before [Eqs. (2a) and (2b)] the total kinetic energy release (KER) is divided between the iodine and methyl fragment in a 15:127 ratio. Therefore the image size for a given KER will differ by a factor of $R(I)/R(CH_3)=[T(I)/T(CH_3)]^{1/2}=(15/127)^{1/2}=0.34$.

C. Determination of quantum yield and anisotropy

As pointed out before, the main observables in this experiment (to deconvolute the A band) are the I* quantum yield, Φ^*, and anisotropy parameters β and β^* for the I and I* channel. The radial information of an image yields the speed distribution from which the kinetic energy release (KER) distribution is extracted. In the state selective $CH_3(v=0)$ images two rings appear, the slow channel (inner ring) corresponding to I* production and the fast to I (outer ring). The two rings do not overlap, which allows an accurate determination of the I* quantum yield $\Phi^*(v=0)$ for $CH_3(v=0)$ (Q branch detection). In an analogous way the KER spread in I and I* images reflects the rovibrational excitation of the corresponding CH_3 fragments.

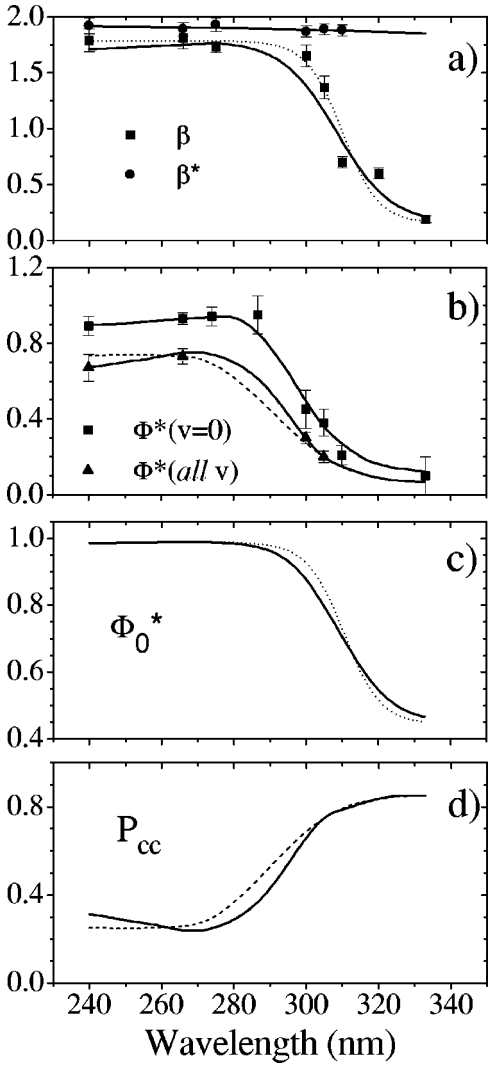

FIG. 3. Dissociation laser wavelength dependence of: (a) experimental anisotropy parameters β and β^*; (b) experimental quantum yield $\Phi^*(v=0)$ from CH_3 images and overall quantum yield Φ^* from iodine REMPI detection; (c) Φ_0^*, corresponding to the amount of parallel absorption from Eq. (8), and (d) the curve crossing probability P_{cc} from Eq. (7).

As discussed later, the most reliable values of β and β^* for the I and I* channel are found from the I and I* images, which can be determined separately without complications due to alignment effects.[12] The $CH_3(v=0)$ images can also provide quantitative data when setting the polarization of the detection laser at the magic angle (54.7°) thereby eliminating possible alignment effects, but large population differences between the I and I* channels cause a sensitivity problem mainly for the I channel, especially for dissociation wavelengths less than ~280 nm. The *overall* yield Φ^* (*all* v) for several dissociation wavelengths is determined from repeated wavelength scans across iodine atom (2+1) REMPI resonances in the 303.5–307 nm region. This approach was more successful compared to determination of the yield from

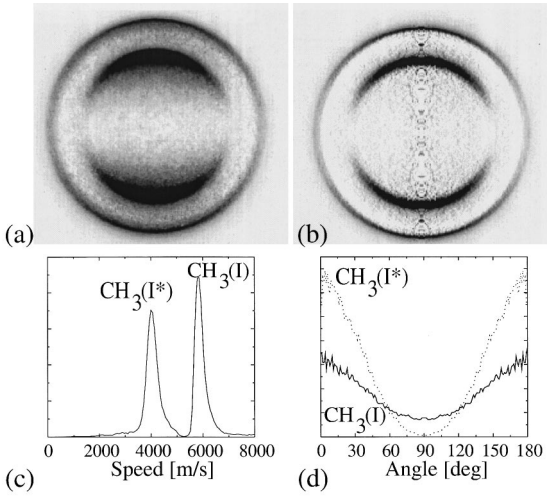

FIG. 4. $CH_3(v=0)$ raw image (a), and Abel inverted image (b) at 305 nm dissociation, 333 nm 0_0^0 Q branch detection; the two peaks in the speed distribution (c) correspond to I and I* formation for which the corresponding angular distributions are plotted in (d).

methyl images, due to the difficulty in detecting CH_3 in all possible vibrational states using REMPI and uncertainties about the vibrational distributions. Still, these data provide a valuable comparison with previous work and are also presented.

IV. RESULTS

Figure 3 shows the main experimental results of this study. Anisotropy parameters, $\beta^*(v=0)$, are determined from methyl $(v=0)$ images, and total β, β^*, and Φ^* values are determined from I and I* images for $\lambda_{diss}=240$, 266, 275, 300, 305, 310, 320, and 333 nm. Figure 3(a) shows the anisotropy parameters from the I and I* images and Fig. 3(b) shows the $\Phi^*(v=0)$ values from $CH_3(v=0)$ images (square symbols) and the total Φ^* values from iodine measurements (triangles). The data points are averaged over a large number (>10) of images, which define the error bars.

A. Anisotropy parameters

1. Methyl (v=0) measurements

For the I* channel, which is dominant for wavelengths shorter than ~290 nm (the most intense part of the absorption spectrum), $v=0$ is the most populated vibrational state of the methyl radical. Most of the qualitative trends of the photodissociation process are evident from the methyl ($v=0$) data in Fig. 3(b), but quantitative analysis requires a number of difficult correction factors, as discussed later. In Fig. 4(a) the velocity image of $CH_3(v=0)$, detected at 333.45 nm (Q bandhead), is shown for 305 nm dissociation. Next to the raw data, the Abel inverted (reconstructed) image is also shown [Fig. 4(b)] from which the speed distribution and angular distributions are extracted [Fig. 4(c),(d)]. The speed distribution for $CH_3(v=0)$ shows the two channels corresponding to I and I*. The sharpness of the two peaks is reduced by the rotational envelope[25,26] (~114 cm^{-1}) of the probed $(v=0)$ rotational distribution (which is assumed to be probed for all rotational states in the Q branch) and also by the apparatus function. Further broadening, especially visible in the horizontal axis of the images shown is not an artifact, it is attributed to dissociation of initially excited vibrational modes of CH_3I, which remain populated since the parent beam is weakly cooled to avoid cluster formation. A more detailed analysis of the CH_3 KER profiles will be presented in a separate article.[5]

By integrating over each peak in the KER spectrum, the $\Phi^*(v=0)$ quantum yield is found for CH_3 in its vibrational ground state, Fig. 3(b). From the angular distributions of the I and I* channel, values of the anisotropy parameters β and β^* are determined using a least-squares fit routine to Eqs. (4). As is seen from these images, the anisotropy in the I* channel displays nearly pure parallel character ($\beta\sim2$) while the I channel has significantly more perpendicular character. Still, the I channel is predominately parallel ($\beta>0$), which implies that most of the I signal originated from $^3Q_0\rightarrow{}^1Q_1$ curve crossing.

2. Iodine measurements

Because iodine images are taken selectively for I and I* fragments, they display a single channel (i.e., I or I*) that corresponds to all correlated methyl fragments. These images are especially suited for extraction of anisotropy parameters β and β^*, Fig. 3(a), since the angular distributions are not affected by fragment alignment and the detector gain can be separately optimized when there are large differences in the I/I* yield. In addition, the iodine speed distribution is determined at a high enough velocity resolution to yield valuable information about the methyl internal energy distribution. In general, the β values presented in Fig. 3(a) agree well with previous I atom REMPI measurements. Powis and Black,[27] for example, reported values of $\beta(I)=1.75\pm0.03$, and $\beta(I^*)=1.95\pm0.03$ for dissociation at 278 nm, while Loo *et al.*[26] find values of $\beta(I^*)=1.8\pm0.1$ and $\beta(I)=1.7\pm0.1$ at 266 nm.

As expected, the I* channel shows parallel character (β^* almost 2) across the full A band, while the I channel displays mixed character leading to lower values of β at longer wavelengths. Two curves (solid and dotted) drawn through the data points of Fig. 3(a) will be used to characterize $\beta(\lambda)$. Clearly, β becomes smaller above 300 nm, indicative of a larger perpendicular contribution in the I channel in the long red tail of the A band.

B. I* quantum yield

At this point the question arises as to what is the most reliable experimental approach for a clear determination of the *overall* I* quantum yield, thus *irrespective of the internal state of the corresponding methyl fragment*. Obviously, the most direct method is by ionization without state selectivity, as achieved ideally in electron-impact time-of-flight mass spectrometry (TOFMS).[18] Using (2+1) REMPI (as in our experiment) the methyl images show directly the I/I* branching, but only for the vibrational state probed; or, the iodine images (either probing I or I*) show the signal intensity for all corresponding methyl fragments, where the sensitivity is determined mainly by the two-photon absorption strength in-

TABLE I. Methyl umbrella mode vibrational distributions at various dissociation wavelengths.

Channel	IR (Ref. 29) 248 nm	TOFMS (Ref. 30) 248 nm	REMPI (Ref. 26) 266 nm	This study 266 nm	5D (Ref. 31) 248 nm	Bent pseudo (Ref. 32) 248 nm	Classical trajectory (Ref. 33) 248 nm
I* $v=0$	0.66	0.65	0.36	0.76[a]	0.79	0.52	0.74
$v=1$	0.26	0.28	0.32	0.15	0.20	0.38	0.19
$v=2$	0.08	0.06	0.32	0.004	0.01	0.09	0.06
$v=3$	0.004	0.01			0.003	0.01	0.01
I $v=0$		0.24			0.27	0.13	0.14
$v=1$		0.34			0.56	0.35	0.32
$v=2$		0.23			0.16	0.32	0.37
$v=3$		0.13			0.01	0.14	0.11
$v=4$		0.04				0.05	0.04
$v=5$		0.02				0.01	0.02

[a]There is also a CH_3I hot band contribution of 0.085.

volved in the REMPI process. In both approaches the total yield has to be determined indirectly, either from a combination of images or from signal intensities which are corrected for transition strengths.

1. Extraction from methyl images

By detecting the methyl fragment using REMPI the I/I* ratio and thus the I* yield could possibly be determined for each vibrational state populated and then averaged over the full vibrational distribution to obtain the overall I* quantum yield. Unfortunately, the I/I* ratio for each umbrella mode (ν_2) excited state is not quantitative since it depends strongly on the exact REMPI detection wavelength, as found before by Loo *et al.*[26] An unambiguous determination of the exact position of the 2_1^1, 2_2^2, and 2_3^3 Q branch is also difficult.[28] At the band maxima, the yield $\Phi^*(\nu_2)$ was found in this study to be 0.94, 0.83, and 0.51 for $\nu_2=0$, 1, and 2 at 266 nm dissociation; these values follow the same trend seen by Loo *et al.*[26] (0.92, 0.77, 0.47) as well as Chandler *et al.*[25] $\Phi^*(v=0)=0.89$, $\Phi^*(\nu_2=1)=0.73$. In recent IR emission[29] and REMPI studies at 266 or 248 nm dissociation wavelengths, the ν_2 umbrella mode distribution is found to be noninverted in the I* channel and inverted in the I channel, peaking at $\nu_2=2$ at 266 nm dissociation. These findings are in agreement with our results, which show a distinctly lower Φ^* when detecting CH_3 in higher umbrella mode states. In principle, the overall yield can be found from these values by taking the weighted summation $\Sigma N_i\Phi^*(\nu_2=i)$ but this requires accurate values of the umbrella mode vibrational distribution N_i (which varies widely in the literature, see Table I) and also requires accurate values of the partial yields $\Phi^*(\nu_2)$. Moreover, the summation does not extend over the total number of states that are presumably produced and the values of the yield obtained in this manner are highly disputable, as discussed in Ref. 26.

Φ^* yields determined by summing partial $\Phi^*(\nu)$ yields can also be compared with our data shown in Fig. 4(b). Loo *et al.*[26] estimated $\Phi^*=0.73$ at 266 nm, based upon $\Phi^*(v=0)=0.92$, $\Phi^*(\nu_2=1)=0.77$, and $\Phi^*(\nu_2=2)=0.47$, assuming a 1.1:1:1 population for $\nu_2=0$, 1, and 2. For comparison, Chandler *et al.*[25] reported at 266 nm $\Phi^*(v=0)=0.89$ and $\Phi^*(\nu_2=1)=0.73$. The higher value [$\Phi^*(v=0)=0.92$] is in good agreement with our data, and the summation ($\Phi^*=0.73$) yields at 266 nm the same value found from iodine images (discussed later).

A simpler way to obtain the total yield from the methyl images could be based upon the $\Phi^*(v=0)$ data only, provided one knows the fraction of fragments that are in $v=0$ for both the I and I* channel. If we denote these fractions by $f(v=0)$ and $f^*(v=0)$, respectively, (where the total contribution of it each channel is normalized to 1.0), the corrected branching ratio is found from

$$\frac{N^*}{N}=\frac{f(v=0)N^*(v=0)}{f^*(v=0)N(v=0)},$$

$$=\frac{f(v=0)\Phi^*(v=0)}{f^*(v=0)[1-\Phi^*(v=0)]}, \tag{10}$$

leading to the corrected overall quantum yield

$$\Phi^*=\frac{(N^*/N)}{1+(N^*/N)}. \tag{11}$$

This approach works, provided one knows the fractions $f(v=0)$ and $f^*(v=0)$ for each dissociation wavelength, thus again requiring accurate vibrational distributions. In this respect, literature cannot provide consistent values, especially across the full range of the A band. In fact, the most reliable data[30] for this calculation, presented in column 2 of Table I. is from a TOF study of the dissociation of CH_3I at 248 nm with electron-impact detection which is unfortunately still unpublished. Using these data [$f(v=0)=0.24$, $f^*(v=0)=0.65$, $\Phi^*(248\text{ nm})=0.73$], and Eqs. (10), (11), a value of $\Phi^*(v=0)(248\text{ nm})=0.84$ is predicted, which is somewhat lower but within the error limits of the value $\sim$0.90 interpolated from the $\Phi^*(v=0)$ [curve in Fig. 3(b)]. None of the other previous experimental determinations of $f,f^*(\nu_2)$ directly resolved the umbrella mode distributions, and most assumed a too-low value for D_0. Apart from the widely fluctuating, and often miscalibrated, $f,f^*(\nu_2)$ results from the various studies at different wavelengths, no account has been taken for other vibrational modes in the methyl radical, and, as shown later on, especially the $\nu_1=1$ vibration cannot be disregarded at short dissociation wavelengths. Furthermore, a sizable fraction of the methyl radicals can

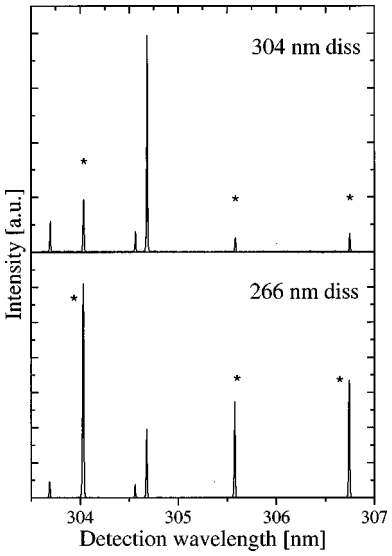

FIG. 5. Iodine (2+1) REMPI spectra, (a) using a single laser at ~304 nm, and (b) with a 266 nm dissociation laser added, showing just the double-resonant signal. Signal intensities are corrected for quadratic laser power dependence. The lines denoted with an asterisk (*) correspond to I* resonances, the others to I. See also Table II.

have vibrationally hot methyl iodide as a precursor, which also affects the relative product yields. To illustrate this, data from the internal energy analysis of the velocity images[5] are presented in column 5 of Table I. Thus while the data from this study does agree reasonably with the most reliable previous data at 266 and 248 nm, we conclude that determination of the I* yield from methyl images is too uncertain.

2. Extraction using iodine REMPI signals

The integrated signal intensities of iodine (2+1) REMPI resonances are preferred for determining the overall yield. Figure 5 shows two I^+ spectra obtained with a photomultiplier which integrates the signal from the phosphor screen of the imaging detector. Both traces are corrected for a quadratic power dependence of the detection laser intensity, which varied by <15% across the full 303.5–307 nm range. Lines with an asterisk (*) denote I* resonances. The upper trace, Fig. 5(a), was obtained with a single laser (~305 nm) and the lower trace, Fig. 5(b), includes a 266 nm dissociation laser (showing just the double resonant signal). As expected, at 266 nm the I* lines are much higher compared to 305 nm.

Repeated scans were recorded across a few close-lying I and I* resonances of comparable strength, by turns with and without dissociation laser at 240, 266, and 300 nm and with careful pressure scanning of an etalon in the dye laser oscillator (~0.05 cm^{-1} bandwidth). In this way the detection laser intensity could be kept sufficiently constant (which was checked with the single laser intensities) and pure double resonant signals could be extracted. In Table II the two-photon line strengths have been calibrated by setting $\Phi^*=0.73$ at 266 nm, based upon time-of-flight mass spectrometer TOFMS[34] and IR[35] results. [Note that quantum yields from TOFMS are much more reliable than $\Phi,\Phi^*(\nu_2)$ values.] Using these line strengths, the experimental values for Φ^* in Fig. 3(b) have been found. For comparison with Φ^* yield results obtained previously, a summary is given in Table III.

TABLE II. (2+1) REMPI lines for I and I* atoms.

Iodine state	λ_{det} (nm)	Intermediate State	Two-photon line strength[a]
$I(^2P_{3/2})$	303.68	$6p\ ^4P_{1/2}$	4.37
$I^*(^2P_{1/2})$	304.02	$6p\ ^4D_{1/2}$	0.90
$I(^2P_{3/2})$	304.55	$6p\ ^4D_{7/2}$	5.18
$I(^2P_{3/2})$	304.67	$6p\ ^2D_{5/2}$	1.00
$I^*(^2P_{1/2})$	305.57	$6p\ ^2P_{3/2}$	2.00
$I^*(^2P_{1/2})$	306.73	$6p\ ^2D_{3/2}$	1.63

[a]Calibrated using $\Phi^*(266\ nm)=0.73$, from Refs. 34,35.

TABLE III. I* quantum yields.

Wavelength (nm)	Φ^*	Ref.
222	0.63±0.02	40
248	0.81±0.03	41
	0.73	30
	0.71±0.02	42
	0.70	43
	0.73	44
	0.58	39
	0.81	45
	0.89/0.67[a]	32
266	0.73±0.04	35
	0.76	34
	0.77	39
	0.89/0.79[a]	32
	0.68	38
F.C.[b]	0.83/0.87[a]/0.72[c]	32
	0.91	46
304	0.43	38
	0.20[d]	36
333	0.10	47

[a]Includes $^1Q_1$ absorption.
[b]Calculated for Franck–Condon overlap with the full PE curve.
[c]Includes $^1Q_1$ absorption based on MCD analysis
[d]Corrected value, see text.

Φ^* yields were extracted from REMPI measurements in a similar study at ~304 nm by Kang *et al.*[36] These authors determined Φ^* using REMPI of iodine, in combination with a pulsed-field time-of-flight detection method with a discriminating pinhole in front of the detector. They used the I* and I REMPI resonances at 304.02 and 304.67 nm, respectively, and determined a line strength ratio of I*:I of 0.80 ±0.05, as calibrated using an I_2 photolysis process which yields equal amounts of I and I*. Our value of 0.90 is quite near theirs (see Table III). They also report an I* yield of 0.30 at 304 nm, but their formula for the efficiency of the discrimination pinhole did not take into account the angular distributions; using an improved description,[37] their quantum yield becomes 0.20 around 304 nm, which coincides with our value. Hertz and Syage[38] estimate of 0.43 at the same wavelength, employing a pinhole-field deflection method.

At shorter wavelengths good agreement is found with previous studies. Van Veen *et al.*[42] reported $\Phi^*=0.71\pm0.02$ at 248 nm; Riley and Wilson[34] found $\Phi^*=0.76$ at 266 nm. Recently, Φ^* values at 333 nm[47] and 222 nm[40] have been

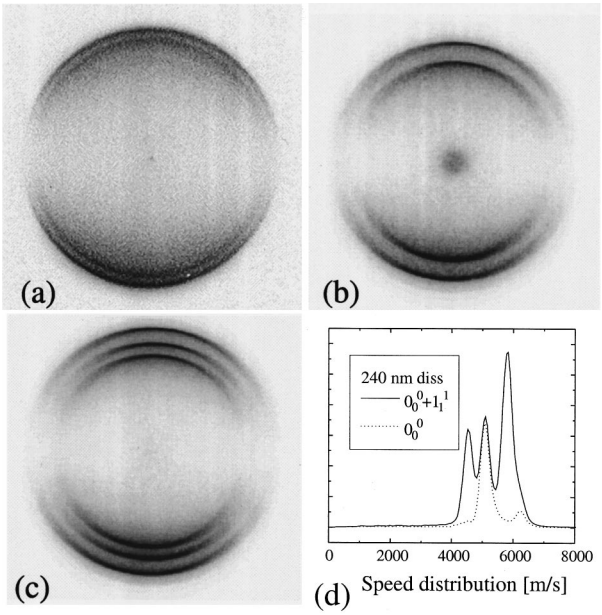

FIG. 6. ν_1 activity at 240 nm dissociation. (a) Raw I image showing two rings for $\nu_1=1$ (inner ring) and $v=0$ (outer ring); (b) Raw CH_3 image at 1_1^1 Q branch detection and 266 nm dissociation, and (c) at 240 nm dissociation; (d) CH_3 speed distributions at 240 nm dissociation on top of the 1_1^1 Q branch [solid curve, 0_0^0 and 1_1^1 contributions, corresponding to the image in panel (c)] and scanned away from 1_1^1 Q branch (dotted curve, only the 0_0^0 contribution).

reported from iodine yields experiments. The later study could be influenced by cluster formation, however, which we observed at 220 nm dissociation: the CH_3^+ appeared here only as a low KER ''blob'' centered in the image. Another CH_3 study at 229 nm[47] did not report quantum yields, but did find a high value of β^* in agreement with our data at 240 nm.

On the theoretical side Hammerich *et al.*[31] and Guo[32] studied the wavelength dependency of the Φ^* yield. Hammerich *et al.* found a yield which is constant over the short wavelengths, with a broadband value of 0.917 (0.916 at the absorption maximum), which drops from 0.92 at 280 nm to 0.67 at 307 nm, and, decreasing even faster, down to 0.05 at 321 nm. Guo predicted quite an analogous behavior when just considering absorption to the $^3Q_0$ state; by including $^1Q_1$: $^3Q_0=0.17:0.81$ absorption (based upon the MCD analysis), Guo finds the yield to increase from ~0.4 at 220 nm to ~0.87 at 300 nm. This behavior is in clear contrast with our data. Despite the fact that the calculated yield is too high at shorter wavelengths, and the predicted drop to lower values is somewhat sharper than experiment, the general behavior is in agreement with the models that do not include a $^1Q_1$ contribution to the initial photoabsorption.

C. ν_1 activity

The excitation of the symmetric stretch vibration (ν_1) of the methyl radical fragment (vibrational energy[48] around 3004 cm^{-1}) following CH_3I photodissociation has been reported previously.[1,2,25,26,49] Vibrational excitation in this mode can be characterized using the higher resolution in velocity imaging. This allows for the first time a quantitative measurement of the ν_1 activity using KER profiles. The I image in Fig. 6(a) at 240 nm dissociation shows two close-lying rings, corresponding to $CH_3(v=0)$ and $(\nu_1=1)$. The I* image data (not shown here) also exhibit a smaller extra ring, indicating a much weaker $\nu_1=1$ signal compared to $v=0$. Since in energy $1\nu_1\sim4\nu_2$ (=2908 cm^{-1}), the umbrella mode vibrational progression in the I channel does not seem to extend very much beyond $\nu_2=4$.

Also shown in Fig. 6(b) and 6(c) are CH_3 images at the 1_1^1 Q branch at 266 and 240 nm dissociation. Since the 1_1^1 Q branch partially overlaps the $P(4)$ branch of the stronger 0_0^0 band,[44] these images have four possibly contributing channels, i.e., I and I* channels with the methyl in $v=0$ and $\nu_1=1$. The three strong channels in Fig. 6(c) at 240 nm correspond to I*$(\nu_1=1)$, I*$(v=0)$, and I$(\nu_1=1)$ for increasing KER, while the weak I$(v=0)$ channel can be discerned at the outer edge. At 266 nm [Fig. 6(b)] only two strong channels appear, corresponding to I*$(v=0)$ and I$(\nu_1=1)$, indicating a higher propensity for the I channel for the CH_3 $(\nu_1=1)$ fragments at 266 nm. As all channels clearly represent parallel character, the initial photoabsorption processes are dominated by the $^3Q_0$ state. From these data, the quantum yield $\Phi^*(\nu_1=1)$ is 0.36 and <0.2 for 240 and 266 nm, respectively. In total, at 240 nm a 15% ν_1 activity is found, which indicates this should be taken into account when considering the energy partitioning. At 266 nm the total ν_1 activity is <5%. This considerably lower activity is confirmed by the rotational band contours showing a weaker 1_1^1 band at 266 nm dissociation. This is in agreement with findings of others: Chandler *et al.*[25] reported I/I*$(\nu_1=1)>2.0$ at 266 nm and early calculations of Amamatsu *et al.*[45] also show a preference for ν_1 activity in the I channel. While no values have been reported on total ν_1 activity, a value of $E_{vib}>0.5\%$ ν_1 was estimated in Ref. 2.

D. CH_3I *A* band decomposition

Using Eqs. (7) and (8), the probability for curve crossing P_{cc} and Φ_0^*, which will be used to represent the *relative* absorption strength, can be found from β, β^* and Φ^*. In Fig. 3(c),(d) these quantities are shown as a function of dissociation wavelength, where the dotted and dashed curves follow from alternative interpolations between the input data points, with distinctive similarities between the curves in panels (a) and (c) on one hand and (b) and (d) on the other. Panel (c) contains no dashed curve and (d) no dotted curve since these ''cross'' dependencies are found to be negligible.

In the short wavelength region up to ~280 nm, Φ_0^* displays a constant behavior close to unity. In other words, the initial photon absorption step is dominated by the parallel transition to the $^3Q_0$ state in this wavelength region. Looking at the curves for P_{cc}, Fig. 3(d), the probability for curve-crossing is about 0.25 in this region. The dashed interpolation would seem intuitively more correct, from a Landau–Zener type of crossing probability: the further away from the crossing point, the faster the crossing speed and the lower the curve crossing probability. The Φ^* data allow for this interpretation within the error bars, but a slightly different behav-

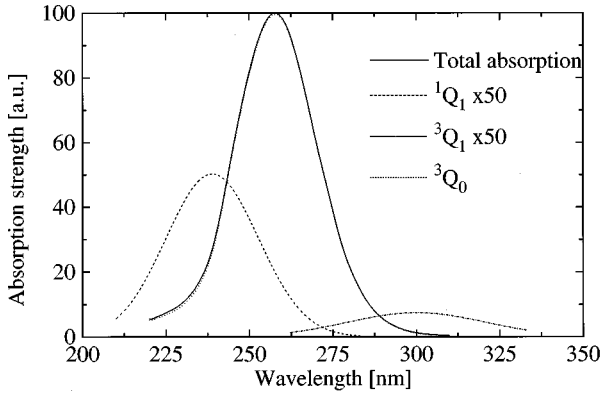

FIG. 7. Experimental absorption spectrum from Ref. 4, and the spectral decomposition into the three contributing states; the two perpendicular states contribute much less and are displayed at 50× magnification.

ior is indicated by the solid line, which passes through the data points more closely.

Above 280 nm, the curves change drastically, with Φ_0^* dropping dramatically and P_{cc} rising toward 0.85. Clearly, an increasing fraction of the absorption is caused by the perpendicular transition to the $^3Q_1$ state; the $^1Q_1$ state absorption strength is negligible in this region. Meanwhile, more curve-crossing takes place when moving toward the conical intersection. Both trends explain the change of appearance in the methyl images, where the outer ring becomes stronger in intensity and displays more perpendicular character (see Fig. 4).

Toward 333 nm the images show nearly pure I channel ($\Phi^*<0.1$), but the $\beta\sim0$ indicates still a large parallel contribution. Therefore, the initial absorption still contains a parallel contribution, which subsequently curve crosses for the main part. The fact that P_{cc} does not show a maximum and distinct decrease could even indicate that the conical intersection between the $^3Q_0$ and $^1Q_1$ potential energy surface (PES) lies at a lower energy. Recent calculations[2] show a quite parallel behavior of the PES with the $^3Q_0$ curve showing a very shallow well, which makes the actual crossing point hard to determine accurately.

One could argue for different explanations for why the anisotropy decreases at longer wavelengths, e.g., molecular rotation competing with slower dissociation, or severe H_3C–I angle bending near the conical intersection. However, the timescale for dissociation is never reported to differ much across the *A* band,[20] and is not very likely due to the steepness of the PES.[2,50] Calculations show no indication for severe angle bending upon curve-crossing. However, despite the fact theory has reached such a supreme level, there are still strong and basic discrepancies with experiment, most importantly, the inability to reproduce the experimental absorption curve. This complicates the interpretation of photodissociation events on basis of these calculations.

In order to construct the decomposed *absolute* absorption spectrum, the experimental absorption spectrum has to be combined with the Φ_0^* yield for the $^3Q_0$ state, and with $(1-\Phi_0^*)$ for the $^1Q_1$ and $^3Q_1$ states. In Fig. 7, a decomposed spectrum shown is based upon the Gedanken and Rowe absorption data. The $^3Q_0$ curve nearly coincides with the total absorption curve. The $^1Q_1$ and $^3Q_1$ curves are displayed at 50×magnification. Although the $^1Q_1$ state contributes more strongly than the $^3Q_1$, its peak value is just 1.0% of the $^3Q_0$ peak, the major component. The $^3Q_1$ peak value is 0.15%, indeed very much weaker than the $^3Q_0$ contribution. Figure 7 should be compared with the deconvoluted spectrum of Gedanken and Rowe,[4] shown schematically as an insert in Fig. 1. The present deconvolution suggests that the MCD data overestimates the $^1Q_1$ component by ~20-fold.

In this analysis the λ_{max} positions (at 240 and 300 nm for $^1Q_1$ and $^3Q_1$, respectively) and the FWHM values for each state were fixed to the values found by Gedanken and Rowe.[4] Each curve was combined with the appropriate Φ_0^* (or $1-\Phi_0^*$) data and a relative strength factor to back-calculate the Φ_0^* curve. It is found that the suggested[4] $^1Q_1$ half-width of 5120 cm^{-1} fits well enough, but the half-width of the $^3Q_1$ state had to be enlarged from 2769 to 4995 cm^{-1} in order to give a good fit. Vibrationally excited CH_3I will contribute mostly in the long wavelength region of the spectrum, however, which could influence the width factors.

Direct absorption studies of CH_3I in a molecular beam have shown a dependence of the CH_3I *A*-band absorption spectrum on the sample temperature.[51] The blue wing in the absorption spectrum is more pronounced at higher temperatures, which has been attributed to dimer formation. In how far the presence of dimers affect the absorption spectrum presented in the MCD analysis, or the MCD analysis itself, is not clear. Performing a similar analysis based upon the ''dimer-free'' red-shifted absorption spectrum (peaking at 262.5 nm), peak values of 1.0% and 0.19% were found for $^1Q_1$ and $^3Q_1$, respectively, using the same λ_{max} and half-widths. The resulting integrated relative strengths of the perpendicular states (1.1% and 0.20% for $^1Q_1$ and $^3Q_1$, respectively), and the quality of the back-calculated fit to Φ_0^* are not influenced much by shifting the absorption curves.

V. CONCLUSION

The decomposed *A*-band absorption spectrum of methyl iodide is shown to be significantly different from that suggested by Gedanken and Rowe[4] in 1975, most importantly in the decreased contribution from the $^1Q_1$ state and the wider apparent width of the $^3Q_1$ state. The Gedanken and Rowe results have been incorporated in a great number of theoretical treatments of methyl iodide photodissociation, and are still often used in the current literature, despite the growing suspicions over the years of the discrepancies which are brought to light in this work. The most important results of this study are the wavelength trends in $\Phi^*(\lambda)$ and $P_{cc}(\lambda)$. $\Phi^*(\lambda)$ should be combined with a quantitative absorption spectrum which is free from absorption by clusters or vibrationally excited molecules. This will yield the most reliable spectral decomposition. An accurate theoretical model should be able to reproduce the measured $P_{cc}(\lambda)$ function, which should also give a good indication for the position of the conical intersection of the $^1Q_1$ and $^3Q_0$ states. The decomposition is based on a very simple assumption of axial recoil and the separation of optical excitation and product

angle-velocity distributions. In a separate study[5] of state-selected CH_3 product angle-velocity distributions we find no strong evidence to contradict this assumption. Vibrationally excited molecules still present in the supersonic expansion are found, however, to contribute to the longest wavelength region of the absorption spectrum (>300 nm). Because the total absorption is quite weak in this region, the absolute contribution of vibrationally excited species to the results of this study is minimal.

ACKNOWLEDGMENTS

This work is part of the research program of the ''Stichting voor Fundamenteel Onderzoek der Materie (FOM),'' which is financially supported by the ''Nederlandse Organisatie voor Wetenschappelijk Onderzoek, (NWO).'' The authors gratefully acknowledge technical assistance from Cor Sikkens.

[1] B. R. Johnson, C. Kittrell, P. B. Kelly, and J. L. Kinsey, J. Phys. Chem. **100**, 7743 (1996).
[2] Y. Amamatsu, S. Yabushita, and K. Morokuma, J. Chem. Phys. **104**, 9783 (1996).
[3] H. Guo and G. C. Schatz, J. Chem. Phys. **93**, 393 (1990).
[4] A. Gedanken and M. D. Rowe, Chem. Phys. Lett. **34**, 39 (1975).
[5] A. T. J. B. Eppink and D. H. Parker, J. Chem. Phys. (submitted).
[6] D. W. Chandler and P. W. Houston, J. Chem. Phys. **87**, 1445 (1987).
[7] A. J. R. Heck and D. W. Chandler, Annu. Rev. Phys. Chem. **46**, 335 (1995).
[8] P. L. Houston, J. Phys. Chem. **100**, 12757 (1996).
[9] A. T. J. B. Eppink and D. H. Parker, Rev. Sci. Instrum. **68**, 3477 (1997).
[10] D. H. Parker and A. T. J. B. Eppink, J. Chem. Phys. **107**, 2357 (1997).
[11] A. T. J. B. Eppink, D. H. Parker, M. H. M. Janssen, B. Buijsse, and W. J. van der Zande, J. Chem. Phys. **108**, 1305 (1998).
[12] M. H. M. Janssen, D. H. Parker, G. O. Sitz, S. Stolte, and D. W. Chandler, J. Phys. Chem. **95**, 8007 (1991).
[13] T. N. Kitsopolous, M. A. Buntine, D. P. Baldwin, R. N. Zare, and D. W. Chandler, Science **260**, 1605 (1993).
[14] J. W. G. Mastenbroek, C. A. Taatjes, K. Nauta, M. H. M. Janssen, and S. Stolte, J. Phys. Chem. **99**, 4360 (1995); see also, D. Y. Kim, N. Brandstater, L. Pipes, T. Garner, and D. Baugh, *ibid.* **99**, 4364 (1994).
[15] R. S. Mulliken, J. Chem. Phys. **8**, 382 (1940).
[16] M. Tadjeddine, J. P. Flament, and C. Teichteil, Chem. Phys. **118**, 45 (1987).
[17] C. E. Moore, *Atomic Energy Levels* (Natl. Stand. Ref. Data. Ser., Natl. Bur. Stand. Cir. 35, U.S. Govt. Printing Office, Washington, D.C. 1971), Vol. III.
[18] R. E. Continetti, B. A. Balko, and Y. T. Lee, J. Chem. Phys. **89**, 3383 (1988).
[19] Q. Zhu, J. R. Cao, Y. Wen, J. Zhang, X. Zhong, Y. Huang, W. Fang, and X. Wu, Chem. Phys. Lett. **144**, 486 (1988).
[20] M. Dzvonik, S. Yang, and R. Bersohn, J. Chem. Phys. **61**, 4408 (1974); D. Zhong, P. Y. Cheng, and A. H. Zewail, *ibid.* **105**, 7864 (1996).
[21] S. Yabashita and K. Morokuma, Chem. Phys. Lett. **153**, 517 (1988).
[22] K. Q. Lao, M. D. Person, P. Xayariboun, and L. J. Butler, J. Chem. Phys. **92**, 823 (1990).
[23] J. W. Hudgens, T. G. DiGiuseppe, and M. C. Lin, J. Chem. Phys. **76**, 2399 (1982).
[24] A. Gedanken, M. B. Robin, and Y. Yafet, J. Chem. Phys. **76**, 4798 (1982).
[25] D. W. Chandler, J. W. Thoman, Jr., M. H. M. Janssen, and D. H. Parker, Chem. Phys. Lett. **156**, 151 (1989); D. W. Chandler, M. H. M. Janssen, S. Stolte, R. N. Strickland, J. W. Thoman, Jr., and D. H. Parker, J. Phys. Chem. **94**, 4839 (1989).
[26] R. Ogorzalek Loo, H. P. Haerri, G. E. Hall, and P. L. Houston, J. Chem. Phys. **90**, 4222 (1989); R. Ogorzalek Loo, G. E. Hall, H. P. Haerri, and P. L. Houston, J. Phys. Chem. **92**, 5 (1988).
[27] J. F. Black and I. Powis, Chem. Phys. **125**, 375 (1988).
[28] D. H. Parker, Z. W. Wang, M. H. M. Janssen, and D. W. Chandler, J. Chem. Phys. **90**, 60 (1989).
[29] T. Suzuki, H. Kanimori, and E. Hirota, J. Chem. Phys. **94**, 6607 (1991).
[30] Q. Zhu, R. E. Continetti, X. Zhao, B. Balko, E. Hintsa, and Y. T. Lee (unpublished results reported in Ref. 32).
[31] A. D. Hammerich, U. Manthe, R. Kosloff, H. D. Meyer, and L. S. Cederbaum, J. Chem. Phys. **101**, 5623 (1994).
[32] H. Guo, J. Chem. Phys. **96**, 6629 (1992).
[33] Y. Amamatsu, K. Morokuma, and S. Yabushita, J. Chem. Phys. **94**, 4858 (1991).
[34] S. J. Riley and K. R. Wilson, Faraday Discuss. Chem. Soc. **53**, 132 (1972).
[35] W. P. Hess, S. J. Kohler, H. K. Haugen, and S. R. Leone, J. Chem. Phys. **84**, 2143 (1986).
[36] W. K. Kang, K. W. Jung, D. C. Kim, and K. H. Jung, J. Chem. Phys. **104**, 5815 (1996).
[37] The detection efficiency, F, of a discrimination pinhole, with the dissociation laser polarized parallel to the TOF axis, becomes: $F=(1-\frac{1}{2}\beta)(1-\cos\theta_{\max})+\frac{1}{2}\beta(1-\cos^3\theta_{\max})$, where $\theta_{\max}=\sin^{-1}(v_d/v)$ with β the anisotropy parameter for the iodine atom (=1.4), v the recoil velocity of the iodine atom (=474 m/s), and v_d the radius of the discrimination hole in the velocity domain (=148 m/s). Similarly, a Φ^* can be defined with $\beta^*=1.9$ and $v^*=331$ m/s. Therefore, we find $\Phi/\Phi^*=0.417$ instead of their value (0.685).
[38] R. A. Hertz and J. A. Syage, J. Chem. Phys. **100**, 9265 (1994).
[39] S. Uma and P. K. Das, Chem. Phys. Lett. **241**, 335 (1995).
[40] S. L. Baughcum and S. R. Leone, J. Chem. Phys. **72**, 6531 (1980).
[41] G. N. A. van Veen, T. Baller, A. E. de Vries, and N. J. A. van Veen, Chem. Phys. **87**, 405 (1984).
[42] M. D. Barry and P. A. Gordy, Mol. Phys. **61**, 827 (1987).
[43] F. G. Godwin, C. Paterson, and P. A. Gorry, Mol. Phys. **61**, 827 (1987).
[44] P. Brewer, P. Das, G. Ondrey, and R. Bersohn, J. Chem. Phys. **79**, 720 (1983).
[45] Y. Amamatsu, K. Morokuma, and S. Yabushita, J. Chem. Phys. **94**, 4858 (1991).
[46] D. H. Fairbrother, K. A. Briggman, E. Weitz, and P. C. Stair, J. Chem. Phys. **101**, 3787 (1994).
[47] S. M. Penn, C. C. Hayden, K. J. C. Muyskens, and F. F. Crim, J. Chem. Phys. **89**, 2909 (1988).
[48] N. E. Triggs, M. Zahedi, J. W. Nibler, P. DeBarber, and J. J. Valentini, J. Chem. Phys. **96**, 1822 (1992).
[49] I. Powis and J. F. Black, J. Phys. Chem. **93**, 2461 (1989).
[50] Y. Amamatsu, K. Morokuma, and S. Yabushita, J. Chem. Phys. **94**, 4858 (1991).
[51] D. J. Donaldson, V. Vaida, and R. Naaman, J. Chem. Phys. **87**, 2522 (1987).